

# Multi-Resolution Beta-Divergence NMF for Blind Spectral Unmixing

Valentin Leplat, *Student Member, IEEE*, Nicolas Gillis, *Member, IEEE*, and Cédric Févotte, *Senior Member, IEEE*

**Abstract**—Blind spectral unmixing is the problem of decomposing the spectrum of a mixed signal or image into a collection of source spectra and their corresponding activations indicating the proportion of each source present in the mixed spectrum. To perform this task, nonnegative matrix factorization (NMF) based on the  $\beta$ -divergence, referred to as  $\beta$ -NMF, is a standard and state-of-the-art technique. Many NMF-based methods factorize a data matrix that is the result of a resolution trade-off between two adversarial dimensions. Two instrumental examples are (1) audio spectral unmixing for which the frequency-by-time data matrix is computed with the short-time Fourier transform and is the result of a trade-off between the frequency resolution and the temporal resolution, and (2) blind hyperspectral unmixing for which the wavelength-by-location data matrix is a trade-off between the number of wavelengths measured and the spatial resolution. In this paper, we propose a new NMF-based method, dubbed multi-resolution  $\beta$ -NMF (MR- $\beta$ -NMF), to address this issue by fusing the information coming from multiple data with different resolutions in order to produce a factorization with high resolutions for all the dimensions. MR- $\beta$ -NMF performs a form of nonnegative joint factorization based on the  $\beta$ -divergence. In order to solve this problem, we propose multiplicative updates based on a majorization-minimization algorithm. We show on numerical experiments that MR- $\beta$ -NMF is able to obtain high resolutions in both dimensions for two applications: the joint-factorization of two audio spectrograms, and the hyperspectral and multispectral data fusion problem.

**Index Terms**—nonnegative matrix factorization,  $\beta$ -divergences, data fusion, spectral unmixing, hyperspectral and multispectral data fusion.

## I. INTRODUCTION

SPECTRAL unmixing concerns the techniques used to decompose the spectrum of a mixed signal into a set of source spectra and their corresponding activations. The activations give the proportion of each source spectrum present in the mixed spectrum. More specifically, blind spectral unmixing consists in estimating the source spectra with limited prior information; usually, the only known information is the number of sources. Spectral unmixing techniques are applied in many fields such as in audio and image processing. In this paper, we introduce a flexible framework to perform spectral unmixing by fusing the information coming from multiple data with

different resolutions. We showcase its efficiency on two major applications: audio spectral unmixing and fusion of hyperspectral and multispectral images. For these applications, the input data usually results from a trade-off between two adversarial dimensions. Let us illustrate this assertion in the particular case of audio spectral unmixing that commonly uses the simultaneous time-frequency representation of an input mixed signal. The simultaneous time-frequency representation is here computed with the short-time Fourier transform (STFT). The STFT consists in dividing the time signal into short segments of the same length, in multiplying the segments element-wise by a window function of size  $2F$ , and then in computing the Fourier transform of each windowed segment (only half of the frequency coefficients can be retained thanks to the Hermitian symmetry). Therefore, from an input signal  $u \in \mathbb{R}^T$ , we obtain a complex matrix  $U \in \mathbb{C}^{F \times N}$  called spectrogram. The number of rows corresponds to the frequency resolution. Letting  $f_s$  be the sampling rate, consecutive rows correspond to frequency bands that are  $\frac{f_s}{2F}$  Hz apart. Choosing a particular value for the window length  $2F$  is equivalent to fixing the frequency and the time resolutions. A larger window implies a higher frequency resolution but it comes at the cost of lower temporal resolution. Moreover, the trade-off between detailed frequency and temporal information is due to the fundamental physical limit known as the Heisenberg uncertainty principle. A natural solution is to consider multiple audio spectrograms and fuse them into a product with both high frequency and high temporal resolutions. A similar idea has been studied in the hyperspectral imaging community; see for example [1], [2], [3], [4], [5], [6], [7], [8], [9]. Indeed, hyperspectral (HS) images have high spectral resolution (typically between 100 and 200 spectral bands) but low spatial resolution, whereas the opposite is true for multispectral (MS) images. The fusion of HS and MS data, which we refer to as the HS-MS fusion problem, gives the possibility to produce fused data with both high spectral and high spatial resolutions, called the super-resolution (SR) image. The SR image can improve the precision of the unmixing [10].

Over the last two decades, nonnegative matrix factorization (NMF) [11] has emerged as a useful method to decompose the spectrogram of a mixed audio signal [12], [13], [14], [15]. Indeed, power or amplitude spectrograms of common audio signals, denoted here by  $V$  such that  $V = |U|^2$  or  $V = |U|$ , show two fundamental properties: sparsity and redundancy (due to the repetition of the spectral signature of the elementary sources that compose the signal). Mathematically, we say that the spectrogram has a low-rank structure [16]. Similar observations can be made for multi-bands images as

Department of Mathematics and Operational Research, Faculté Polytechnique, Université de Mons, Rue de Houdain 9, 7000 Mons, Belgium. Authors acknowledge the support by the Fonds de la Recherche Scientifique - FNRS and the Fonds Wetenschappelijk Onderzoek - Vlanderen (FWO) under EOS Project no 0005318F-RG47, and by the European Research Council (ERC Starting Grant no 679515). E-mails: {valentin.leplat, nicolas.gillis}@umons.ac.be.

Cédric Févotte is with IRIT, Université de Toulouse, CNRS, Toulouse, France. He acknowledges the support by the European Research Council (ERC Consolidator Grant no 6681839). E-mail: cedric.fevotte@irit.fr.

the spectral signature of each pixel can be seen as a mixture of a few spectral signatures of pure materials present in the image and referred to as endmembers. These two fundamental properties led spectral unmixing problems to integrate low-rank approximation techniques such as NMF, which is well known to extract sparse and meaningful estimates for the source spectra [17], [18]. Given the nonnegative matrix  $V \in \mathbb{R}_+^{F \times N}$  and a positive integer  $K \ll \min(F, N)$  (the factorization rank), NMF aims to compute a nonnegative matrix  $W$  with  $K$  columns and a nonnegative matrix  $H$  with  $K$  rows such that  $V \approx WH$ . The matrix  $W$  is referred to as the dictionary matrix whose columns correspond to the spectral content of a source estimate. The matrix  $H$  is the activation matrix specifying if a source is active at a certain time frame (or at a certain pixel location in the image for the HS-MS fusion problem) and in which intensity.

*Contribution and outline:* In this paper, we propose multi-resolution  $\beta$ -NMF (MR- $\beta$ -NMF) for fusing the information coming from multiple audio amplitude spectrograms with different frequency resolutions. As far as we know, it is the first time such an approach is used in this context. High-frequency-resolution data and high-temporal-resolution data are jointly factorized by MR- $\beta$ -NMF, taking into account the linear mixture model (3). Based on these audio spectrograms, we are able to generate a solution  $W$  that exploits the spectral accuracy from the high-frequency-resolution data and a solution for  $H$  exploiting the temporal accuracy from the high-temporal-resolution data. Both frequency and temporal reconstruction qualities are evaluated by numerical simulation using synthetic audio signals. We also show that MR- $\beta$ -NMF is flexible and can be used in other applications. In particular we motivate and show its efficiency to deal with the HS-MS fusion problem. As far as we know, it is the first time that a HS-MS fusion model and algorithm tackles any  $\beta$ -divergence. Most previous works focused on the case  $\beta = 2$ , that is, least squares, which assumes Gaussian noise as a prior. As we will see, considering  $\beta$ -divergences for  $\beta \neq 2$  allows to obtain much better solutions in the presence of non-Gaussian noise. In particular, we show that in the presence of Poisson noise, using  $\beta = 1$  (Kullback-Leibler divergence) outperforms standard approaches.

This paper is organized as follows. Section II details the problem formulation, in particular the mixture model, the motivation for using NMF, and our proposed MR- $\beta$ -NMF approach. Section III describes the algorithm developed to tackle this problem. Section IV (resp. Section V) presents numerical results on audio datasets (resp. on the HS-MS fusion problem). MR- $\beta$ -NMF is shown to be competitive with state-of-the-art techniques, and allows to obtain solutions with both high spectral resolution and high temporal (resp. spatial) resolution.

## II. PROBLEM FORMULATION

The aim of multi-resolution unmixing, or more generally data fusion, is to estimate non-observable data with high resolutions in adversarial dimensions from observable data that show high resolution in one dimension only. In this paper, we

propose a flexible framework that can be easily adapted to many applications. More particularly, we consider the blind audio spectral unmixing and the HS-MS fusion problem.

In the case of the audio spectral unmixing, the multi-resolution unmixing is based on high-frequency-resolution (HRF) data and low-frequency-resolution (LRF) data. In this paper we limit the discussion to the use of two input audio amplitude spectrograms  $X \in \mathbb{R}_+^{F_X \times N_X}$  and  $Y \in \mathbb{R}_+^{F_Y \times N_Y}$ . We assume they are computed with STFTs based on a common input audio signals  $u$ . The windows lengths are respectively  $F_X$  and  $F_Y$  such that  $F_Y > F_X$  with  $\frac{F_Y}{F_X} = d$  where  $d$  is usually referred to as the frequency downsampling ratio. Sizes  $N_X$  and  $N_Y$  denote the number of time frames of LRF and HRF spectrograms, respectively, with  $N_X > N_Y$  as per the trade-off between frequency and temporal resolutions. Given  $X$  and  $Y$ , we are searching for an amplitude audio spectrogram  $V \in \mathbb{R}_+^{F_Y \times N_X}$  that has both high frequency and high temporal resolutions. We suppose in this paper that the observed LRF spectrogram  $X$  is a frequency downsampled version of  $V$ , that is,

$$X \approx RV, \quad (1)$$

where  $R \in \mathbb{R}^{F_X \times F_Y}$  is the frequency downsampling operator. Similarly, the observed HRF spectrogram  $Y$  is a temporally downsampled version of  $V$ , that is,

$$Y \approx VS, \quad (2)$$

where  $S \in \mathbb{R}^{N_X \times N_Y}$  is the temporal downsampling operator. For the HS-MS fusion problem, we assume that a high spatial resolution image  $X$  and a high spectral resolution image  $Y$  are available to reconstruct the target image with high-spectral and high-spatial resolutions  $V$ , the SR image. These images result from the linear spectral and spatial degradations of the SR image  $V$ , given by the same equations (1) and (2). In this context, the operator  $R$  from (1) is the relative spectral bandpass responses from the super-resolution image to the MS image, while the operator  $S$  introduced in (2) specifies the spatial blurring and down-sampling responses that result in the HS image. In the context of HS-MS fusion, the operators  $R$  and  $S$  can be acquired either by cross-calibration [19] or by estimations from the HS and MS images [10], [20]. As far as we know, in the context of audio spectral unmixing, it is unknown how to estimate  $R$  and  $S$ , and we will propose an optimization strategy to do so.

1) *Linear Spectral Mixture Model:* A linear spectral mixture model is commonly used for the audio spectral unmixing or HS unmixing due to its physical meaning and its mathematical simplicity; see [21], [22], [23] for detailed reviews. Under this model the input data matrix  $V$  has the form

$$V \approx WH, \quad (3)$$

where  $W \in \mathbb{R}_+^{F_Y \times K}$  is the dictionary matrix and  $H \in \mathbb{R}_+^{K \times N_X}$  is the activation matrix. In the case of audio spectral unmixing, a column of an amplitude audio spectrogram is then supposed to be a nonnegative linear combination of the amplitude spectrograms of the sources. For HS-MS data fusion, the linear mixture model makes senses as it exploits a natural feature of multi-band images: each spectral vector representing a pixel

can be seen as a linear mixture of several spectral signatures, called endmembers, that correspond to the reflectance of a material at different wavelengths of light. The matrix  $W$  is referred to as the endmember matrix whose columns are spectral signatures, and  $H$  is the abundance matrix whose entries are the abundances of the endmembers in the pixels.

Substituting (3) into (1) and (2),  $X$  and  $Y$  are expressed as follows:

$$X \approx RWH, \quad (4)$$

$$Y \approx WHS. \quad (5)$$

Equations (4) (resp. (5)) correspond to the linear spectral mixture model degraded in the frequency (resp. spectral) and temporal (resp. spatial) domains. This leads to our proposed NMF approach described in the next section.

2) *Multi-Resolution  $\beta$ -NMF*: In this section, we present a new approach for spectral unmixing based on the minimization of  $\beta$ -divergences. To solve the multi-resolution problem and estimate the signal  $V$ , we need to estimate  $W$  and  $H$ . From (4) and (5), we propose to solve the following optimization problem, which we refer to as MR- $\beta$ -NMF:

$$\min_{W \geq 0, H \geq 0, R \geq 0, S \geq 0} D_\beta(X|RWH) + \lambda D_\beta(Y|WHS), \quad (6)$$

where  $A \geq 0$  means that  $A$  is component-wise nonnegative,  $\lambda$  is a positive penalty parameter, and  $D_\beta(Z|ABC) = \sum_{fn} d(Z_{fn}|[ABC]_{fn})$  with  $d(x|y)$  an appropriate error measure between the scalars  $x$  and  $y$ . In the general case, MR- $\beta$ -NMF is also able to estimate the downsampling operators  $R$  and  $S$ , which is a contribution. Note that when the downsampling operators  $R$  and  $S$  are known, the objective function is minimized over  $W$  and  $H$  only, see section III for more details. Note also that in general  $R$  and  $S$  have a particular structure where some entries are fixed to zero; see Section II-3. As our algorithm will rely on multiplicative updates, entries initialized at zero remain zero in the course of the optimization process. In audio spectral unmixing, a common measure of fit is the  $\beta$ -divergence, denoted  $d_\beta(x|y)$ , and equal to

$$\begin{cases} \frac{1}{\beta(\beta-1)} (x^\beta + (\beta-1)y^\beta - \beta xy^{\beta-1}) & \text{for } \beta \neq 0, 1, \\ x \log \frac{x}{y} - x + y & \text{for } \beta = 1, \\ \frac{x}{y} - \log \frac{x}{y} - 1 & \text{for } \beta = 0, \end{cases}$$

where  $x$  and  $y$  are nonnegative scalars. For  $\beta = 2$ , this amounts to the standard squared Euclidean distance since  $d_2(x|y) = 1/2(x-y)^2$ . For  $\beta = 1$  and  $\beta = 0$ , the  $\beta$ -divergence corresponds to the Kullback-Leibler (KL) divergence and the Itakura-Saito (IS) divergence, respectively. The error measure should be chosen depending on the noise statistic assumed on the data. The Euclidean distance assumes i.i.d. Gaussian noise, KL divergence assumes Poisson noise, and the IS divergence assumes multiplicative Gamma noise [24]. KL and IS divergences are usually considered for amplitude spectrogram and power spectrogram, respectively. Both KL and IS divergences are more adapted to audio spectral unmixing than Euclidean distance; see [25] and [12]. The Euclidean distance is the most widely used to tackle the HS unmixing problem as well as the HS-MS data fusion problem. However, when no obvious choice of a specific divergence is available,

finding the right measure of fit, namely the value for  $\beta$ , can be seen as a model selection problem [26]. Therefore an objective function with an adjustable  $\beta$  is fully justified. Moreover, divergences are often log-likelihoods in disguise and therefore choosing a divergence boils down to choosing a noise statistic as mentioned earlier. For example, sensors embedded in cameras can be seen as photon counters, and the Poisson distribution makes particular sense for count data. This assumption supports once again our motivation to consider an adjustable  $\beta$ , in this case with  $\beta = 1$ . Based on numerical experiments, we will show that the KL-divergence is also well suited for the HS-MS fusion problem.

3) *Downsampling operators*: As mentioned earlier, for HS-MS data fusion, downsampling operators can usually be estimated and hence are assumed to be known. In the context of audio spectral unmixing, the downsampling operators in (6) are unknown. Different structures for downsampling operators  $R$  and  $S$  have been tested, and we report here the form for  $R$  that shows the best results in practice, while  $S$  is obtained in the same way. Let us illustrate this on the simple example of the frequency downsampling of a matrix  $W \in \mathbb{R}^{8 \times 3}$  with a downsampling ratio  $d = 2$ . A possible structure for the matrix  $R \in \mathbb{R}_+^{4 \times 8}$  is as follows:

$$R = \begin{pmatrix} \underline{r_{11}} & \underline{r_{12}} & \mathbf{r_{13}} & 0 & 0 & 0 & 0 & 0 \\ 0 & \mathbf{r_{21}} & \underline{r_{22}} & \underline{r_{23}} & \mathbf{r_{24}} & 0 & 0 & 0 \\ 0 & 0 & 0 & \mathbf{r_{31}} & \underline{r_{32}} & \underline{r_{33}} & \mathbf{r_{34}} & 0 \\ 0 & 0 & 0 & 0 & 0 & \mathbf{r_{41}} & \underline{r_{42}} & \underline{r_{43}} \end{pmatrix},$$

This downsampling operator  $R$  performs a weighted arithmetic mean over a set of rows of the matrix it is applied on; here,  $W \in \mathbb{R}_+^{8 \times 3}$  is downsampled as  $RW \in \mathbb{R}_+^{4 \times 3}$ . The structure of the matrix  $R$  relies on two parameters:  $d$  and  $f$ . As mentioned earlier,  $d$  corresponds to the downsampling ratio. Each row of  $R$  has at least  $d$  non-zero values that correspond to the rows in  $W$  that are combined to form the rows of  $RW$ ; see the underlined entries of  $R$  above. The parameter  $f$  controls the overlap between the linear combinations of the rows of  $W$ . In the example above,  $f = 1$  and one positive value is added to the left and the right end of the  $d$  non-zero entries corresponding to the downsampling parameter; see the bold entries in matrix  $R$  above. These positive values allow an overlap (or coupling) within the downsampling process. If we consider two consecutive frequency bins that result from a downsampling operation, it is reasonable to consider that they share common frequency bins in the original frequency space. We imposed  $f \leq d/2$  to avoid too much non-physical coupling. This limitation is also based on numerical experiments that show a degradation of the results when  $f$  exceeds  $d/2$ . When  $f = 0$ , the downsampling operator  $R$  performs a weighted arithmetic mean over  $d$  rows without overlapping. Note that these downsampling operators are sparse nonnegative matrices.

### III. ALGORITHM FOR MR- $\beta$ -NMF

Most NMF algorithms are based on an iterative scheme that alternatively update  $H$  for  $W$  fixed and vice versa, and we adopt this approach in this paper. Note that the  $\beta$ -divergence is only convex with respect to its second argument when  $\beta \in$

[1, 2]. The goal in this section is to derive an algorithm to solve MR- $\beta$ -NMF (6).

For  $R, S$  and  $W$  fixed, let us consider the subproblem in  $H$ :

$$\min_{H \geq 0} L(H) = D_\beta(X|RWH) + \lambda D_\beta(Y|WHS). \quad (7)$$

As we will see, the subproblems in  $W, R$  and  $S$  for the other variables fixed are similar. To tackle this problem, we follow the standard majorization-minimization framework [27]. We start by constructing an auxiliary function denoted  $\bar{L}$  which is a tight upper-bound for the objective  $L$  at the current iterate. An auxiliary function for  $L$  at point  $\tilde{H}$  is defined as follows.

**Definition 1.** The function  $\bar{L}(H|\tilde{H}) : \Omega \times \Omega \rightarrow \mathbb{R}$  is an auxiliary function for  $L(H) : \Omega \rightarrow \mathbb{R}$  at  $\tilde{H} \in \Omega$  if the conditions  $\bar{L}(H|\tilde{H}) \geq L(H)$  for all  $H \in \Omega$  and  $\bar{L}(\tilde{H}|\tilde{H}) = L(\tilde{H})$  are satisfied.

The optimization problem with  $L$  is then replaced by a sequence of simpler problems for which the objective is  $\bar{L}$ . The new iterate  $H^{(i+1)}$  is computed by minimizing the auxiliary function at the previous iterate  $H^{(i)}$ , either approximately or exactly. This guarantees  $L$  to decrease at each iteration.

**Lemma 1.** Let  $H, H^{(i)} \geq 0$ , and let  $\bar{L}$  be an auxiliary function for  $L$  at  $H^{(i)}$ . Then  $L$  is non-increasing under the update  $H^{(i+1)} = \operatorname{argmin}_{H \geq 0} \bar{L}(H|H^{(i)})$ .

*Proof.* By definition,  $L(H^{(i)}) = \bar{L}(H^{(i)}|H^{(i)}) \geq \min_H \bar{L}(H|H^{(i)}) = \bar{L}(H^{(i+1)}|H^{(i)}) \geq L(H^{(i+1)})$ .  $\square$

The most difficult part in using the majorization-minimization framework is to design an auxiliary function that is easy to optimize. Usually such auxiliary functions are separable (that is, there is no interaction between the variables so that each entry of  $H$  can be updated independently) and convex. We will construct an auxiliary function for  $L(H)$  from (7) by a positive linear combination of two auxiliary functions, one for each term of  $L(H)$ .

1) *Separable auxiliary function for the first term of  $L(H)$ :* The function  $D_\beta(X|RWH)$  separates into  $\sum_n D_\beta(x_n|RW h_n)$ , where  $x_n$  and  $h_n$  are the  $n$ th column of  $X$  and  $H$  respectively. Therefore we only consider the optimization over one specific column  $x$  of  $X$  and  $h$  of  $H$ . To simplify notation, we denote the current iterate as  $\tilde{h}$ . We now use the separable auxiliary function presented in [12] which consists in majorizing the convex part of the  $\beta$ -divergence using Jensen's inequality and majorizing the concave part by its tangent (first-order Taylor approximation). Note that the divergence can always be expressed as the sum of a convex, concave, and constant part, such that:

$$d_\beta(x|y) = \check{d}_\beta(x|y) + \hat{d}_\beta(x|y) + \bar{d}_\beta(x|y),$$

where  $\check{d}$  is convex function of  $y$ ,  $\hat{d}$  is a concave function of  $y$  and  $\bar{d}$  is a constant of  $y$ , see [12] for the definition of these terms for different values of  $\beta$ .

By denoting  $RW$  by  $P$  and  $RW\tilde{h}$  by  $\tilde{x}$  with entries  $[RW\tilde{h}]_f = \tilde{x}_f$  for  $f \in [1, F_X]$ , the auxiliary function for  $\sum_f d_\beta(x_f|[Ph]_f)$  at  $\tilde{h}$  is given by:

$$G_X(h|\tilde{h}) = \sum_f \left[ \sum_k \frac{p_{fk}\tilde{h}_k}{\tilde{x}_f} \check{d}_\beta(x_f|\tilde{x}_f \frac{h_k}{\tilde{h}_k}) \right] + \bar{d}_\beta(x_f|\tilde{x}_f) + \left[ \hat{d}_\beta(x_f|\tilde{x}_f) \sum_k p_{fk}(h_k - \tilde{h}_k) + \hat{d}_\beta(x_f|\tilde{x}_f) \right]. \quad (8)$$

Therefore the function

$$G_X(H|\tilde{H}) = \sum_n G_X(h_n|\tilde{h}_n) \quad (9)$$

is an auxiliary function (convex and separable) for  $D_\beta(X|RWH)$  at  $\tilde{H}$  where  $G_X(h|\tilde{h})$  is given by (8).

2) *Separable auxiliary function for the second term of  $L(H)$ :* Let  $\tilde{y}_{fn} = [WHS]_{fn}$  and let us use a result from [12]:

$$G_Y(H|\tilde{H}) = \sum_{f,n} \left[ \sum_{k,j} \frac{(w_{fk}s_{jn})\tilde{h}_{kj}}{\tilde{y}_{fn}} \check{d}_\beta(y_{fn}|\tilde{y}_{fn} \frac{h_{kj}}{\tilde{h}_{kj}}) \right] + \bar{d}_\beta(y_{fn}|\tilde{y}_{fn}) + \hat{d}_\beta(y_{fn}|\tilde{y}_{fn}) + \hat{d}_\beta(y_{fn}|\tilde{y}_{fn}) \sum_{k,j} w_{fk}(h_{kj} - \tilde{h}_{kj})s_{jn}. \quad (10)$$

In [12], the authors show that (10) is an auxiliary function (separable and convex) to  $D_\beta(Y|WHS)$  at  $\tilde{H}$ : by construction  $G_Y(H|\tilde{H})$  is an upper-bound to  $D_\beta(Y|WHS)$  at  $\tilde{H}$  and is tight when  $H = \tilde{H}$ .

3) *Auxiliary function for multi-resolution  $\beta$ -NMF:* Based on the auxiliary functions presented in Sections III-1 and III-2, we can directly derive a separable auxiliary function  $\bar{F}(H|\tilde{H})$  for multi-resolution  $\beta$ -NMF (7).

**Corollary 1.** For  $H \geq 0$ ,  $\lambda > 0$ , the function

$$\bar{L}(H|\tilde{H}) = G_X(H|\tilde{H}) + \lambda G_Y(H|\tilde{H}),$$

where  $G_X$  is given by (9) and  $G_Y$  by (10), is a convex and separable auxiliary function for  $L(H) = D_\beta(X|RWH) + \lambda D_\beta(Y|WHS)$ .

*Proof.* This follows directly from (9) and (10).  $\square$

4) *Algorithm for MR- $\beta$ -NMF:* Given the convexity and the separability of the auxiliary function, the optimum is obtained by canceling the gradient. The derivative of the auxiliary function  $\bar{L}(H|\tilde{H})$  with respect to a specific coefficient  $h_{kz}$ ,

with index  $z$  identifying the same column specified by  $n$  in (8) and specified by  $j$  in (10), is given by:

$$\begin{aligned}\nabla_{h_{kz}} \bar{L} &= \nabla_{h_{kz}} G_X(H|\tilde{H}) + \lambda \nabla_{h_{kz}} G_Y(H|\tilde{H}) \\ &= \sum_f^{F_X} p_{fk} \left[ \tilde{d}'_{\beta} \left( x_{fz} |\tilde{x}_{fz} \frac{h_{kz}}{\tilde{h}_{kz}} \right) + \tilde{d}_{\beta}(x_{fz}|\tilde{x}_{fz}) \right] \\ &\quad + \lambda \sum_f^{F_Y} \sum_n^{N_Y} w_{fk} s_{zn} \left[ \tilde{d}'_{\beta} \left( y_{fn} |\tilde{y}_{fn} \frac{h_{kz}}{\tilde{h}_{kz}} \right) \right. \\ &\quad \left. + \tilde{d}_{\beta}(y_{fn}|\tilde{y}_{fn}) \right].\end{aligned}\quad (11)$$

For  $\beta = 1$ , (11) becomes:

$$\begin{aligned}\nabla_{h_{kz}} \bar{L} &= \sum_f^{F_X} p_{fk} \left[ 1 - \frac{x_{fz} \tilde{h}_{kz} \tilde{x}_{fz}^{-1}}{h_{kz}} \right] \\ &\quad + \lambda \sum_f^{F_Y} \sum_n^{N_Y} w_{fk} s_{zn} \left[ 1 - \frac{y_{fn} \tilde{h}_{kz} \tilde{y}_{fn}^{-1}}{h_{kz}} \right].\end{aligned}\quad (12)$$

We set (12) to zero and get the following closed-form solution for the  $h_{kz}$  coefficient of  $H$ :

$$h_{kz} = \tilde{h}_{kz} \frac{\sum_f^{F_X} p_{fk} x_{fz} \tilde{x}_{fz}^{-1} + \lambda \sum_f^{F_Y} \sum_n^{N_Y} w_{fk} s_{zn} y_{fn} \tilde{y}_{fn}^{-1}}{\sum_f^{F_X} p_{fk} + \lambda \sum_f^{F_Y} \sum_n^{N_Y} w_{fk} s_{zn}} \quad (13)$$

The generalization of the closed-form solution (13) for any  $\beta$  for  $H$  is given in Table I in matrix forms. Table I gives also the closed-form solution for  $W$  which is derived with the same rationale. As mentioned in Section II-2, in the general case, operators  $R$  and  $S$  are unknown. We propose here to derive updates for  $R$  and  $S$  so that these operators can be learned from the data and sensible estimates for  $W$  and  $H$  during the optimization scheme. The updates for  $R$  and  $S$  have been derived in a similar fashion as for matrices  $W$  and  $H$ . For the update of  $R$  for instance, one has simply to note it corresponds to the update of  $W$  where we only keep the terms multiplied by  $\lambda = 1$  and where the roles of  $Y$ ,  $W$ ,  $H$  and  $S$  are exchanged with  $X$ ,  $R$ ,  $W$  and  $H$ , respectively.

Algorithm 1 summarizes our method to tackle (6) which is referred as MR- $\beta$ -NMF. It consists in two optimization loops:

- Loop 1: matrices  $W$  and  $H$  are alternatively updated with downsampling operators  $R$  and  $S$  kept fixed so that we obtain good estimates for  $W$  and  $H$ . The updates are performed for a maximum number of iterations imposed by the parameter MAXITERL1.
- Loop 2: matrices  $W$ ,  $H$ ,  $S$  and  $R$  are alternatively updated so that the algorithm learns the downsampling operators during the optimization process. The maximum number of iterations for loop 2 is controlled by parameter MAXITERL2.

For the HS-MS fusion problem, the operators  $R$  and  $S$  are usually known and therefore the parameter MAXITERL2 is set to zero. In this paper, the second optimization loop is considered only for the audio spectral unmixing application since the operators  $R$  and  $S$  are unknown.

After  $W$  and  $H$  are updated, we normalize  $W$  such that  $\|W(:, k)\|_1 = 1$  for all  $k$ , and we normalize  $H$  accordingly so

that  $WH$  remains unchanged. This normalization is commonly used for NMF-based methods and is mainly performed to remove the scaling degree of freedom. As a convergence condition, we consider the relative change ratio of the cost function  $L$  from (6), namely  $|L^i - L^{i+1}| \leq \kappa L^i$  where  $\kappa$  is a given threshold, and  $i$  is the iteration counter. We also stop the optimization process if the number of iterations exceeds the predefined maximum number of iterations.

---

#### Algorithm 1 Multiplicative updates for MR- $\beta$ -NMF

---

**Input:** A matrix  $X \in \mathbb{R}_+^{F_X \times N_X}$ , a matrix  $Y \in \mathbb{R}_+^{F_Y \times N_Y}$ , an initialization  $H \in \mathbb{R}_+^{K \times N_X}$ , an initialization  $W \in \mathbb{R}_+^{F_Y \times K}$ , a matrix  $R \in \mathbb{R}_+^{F_X \times F_Y}$ , a matrix  $S \in \mathbb{R}_+^{N_X \times N_Y}$ , a factorization rank  $K$ , a maximum number of iterations MAXITERL1, a maximum number of iterations MAXITERL2, a threshold  $\kappa$  and a weight  $\lambda > 0$

**Output:** A rank- $K$  NMF  $(W, H)$  of  $V \approx WH$  with  $W \geq 0$  and  $H \geq 0$ , and operators  $R$  and  $S$  such that  $X \approx RWH$  and  $Y \approx WHS$ .

```

1: % Loop 1
2:  $i \leftarrow 0$ 
3: while  $i < \text{MAXITERL1}$  and  $\left| \frac{L^i - L^{i+1}}{L^i} \right| > \kappa$  do
4:   % Update of matrices  $H$  and  $W$ 
5:   Update  $H$  and  $W$  sequentially; see Table I
6:    $(W, H) \leftarrow \text{normalize}(W, H)$ ,  $i \leftarrow i + 1$ 
7: end while
8: % Loop 2
9:  $i \leftarrow 0$ 
10: while  $i < \text{MAXITERL2}$  and  $\left| \frac{L^i - L^{i+1}}{L^i} \right| > \kappa$  do
11:   % Update of matrices  $H, W, S$  and  $R$ 
12:   Update  $H, W, S, R$  sequentially; see Table I
13:    $(W, H) \leftarrow \text{normalize}(W, H)$ ,  $i \leftarrow i + 1$ 
14: end while

```

---

It can be verified that the computational complexity of the MR- $\beta$ -NMF is asymptotically equivalent to the standard MU for  $\beta$ -NMF, that is, it requires  $\mathcal{O}(FNK)$  operations per iteration.

5) *Parallel computing:* We remark that some of the most computationally intensive steps of the proposed algorithm can be easily ran onto a parallel computation platform. Indeed, the complexity of our multiplicative updates detailed in Table I is mainly driven by the matrix products in which matrix  $S$  is involved. On Matlab for example, we can easily take of advantage of a GPU compatible with CUDA libraries by simply transforming usual arrays into GPU arrays. In our case, on a desktop equipped with a Intel Core i7-8700 CPU and a GeForce RTX 2070 Super GPU, the runtime can be up to 5 times shorter.

## IV. NUMERICAL EXPERIMENTS ON AUDIO DATA SETS

In this section, we perform numerical experiments to validate the effectiveness of MR- $\beta$ -NMF on two synthetic audio data sets.

### A. Experimental setup and evaluation

TABLE I: Multiplicative updates for MR- $\beta$ -NMF.

$$\begin{aligned}
H &= \tilde{H} \odot \left( \frac{[W^T (R^T ((RW\tilde{H})^{(\beta-2)} \odot X) + \lambda ((W\tilde{H}S)^{(\beta-2)} \odot Y) S^T)]}{[W^T (R^T (RW\tilde{H})^{(\beta-1)} + \lambda (W\tilde{H}S)^{(\beta-1)} S^T)]} \right)^{\gamma(\beta)}, \\
W &= \tilde{W} \odot \left( \frac{[(R^T ((R\tilde{W}H)^{(\beta-2)} \odot X) + \lambda ((\tilde{W}HS)^{(\beta-2)} \odot Y) S^T) H^T]}{[R^T (R\tilde{W}H)^{(\beta-1)} + \lambda (\tilde{W}HS)^{(\beta-1)} S^T] H^T} \right)^{\gamma(\beta)}, \\
S &= \tilde{S} \odot \left( \frac{[H^T (W^T ((WH\tilde{S})^{(\beta-2)} \odot Y))] }{[H^T (W^T (WH\tilde{S})^{(\beta-1)})]} \right)^{\gamma(\beta)}, \quad R = \tilde{R} \odot \left( \frac{[(\tilde{R}WH)^{(\beta-2)} \odot X] H^T W^T]}{[(\tilde{R}WH)^{(\beta-1)} H^T] W^T} \right)^{\gamma(\beta)},
\end{aligned}$$

where  $A \odot B$  (resp.  $[A]/[B]$ ) is the Hadamard product (resp. division) between  $A$  and  $B$ ,  $A^{(\cdot\alpha)}$  is the element-wise  $\alpha$  exponent of  $A$ ,  $\gamma(\beta) = \frac{1}{2-\beta}$  for  $\beta < 1$ ,  $\gamma(\beta) = 1$  for  $\beta \in [1, 2]$  and  $\gamma(\beta) = \frac{1}{\beta-1}$  for  $\beta > 2$  [12].

1) *Data*: The proposed technique for joint-factorization of amplitude audio spectrograms is applied to two synthetic audio samples. A dedicated test procedure is presented in Section IV-A2 in order to evaluate the performance of MR- $\beta$ -NMF based on quantitative criteria detailed in subsection IV-A3. The first audio sample is the first measure of “Mary had a little lamb” and composed of three notes;  $E_4$ ,  $D_4$  and  $C_4$ . The signal is 5 seconds long and has a sampling frequency  $f_s = 44100\text{Hz}$  yielding  $T = 220500$  samples.

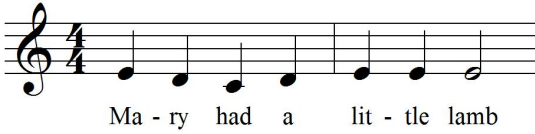


Fig. 1: Musical score of “Mary had a little lamb” (referred as dataset 1).

The second audio sample, inspired from [24], is a piano sequence played from the score given in Figure 2. The piano sequence is composed of four notes;  $D_4$ ,  $F_4$ ,  $A_4$  and  $C_5$ , played all at once in the first measure and then played by pairs in all possible combinations in the remaining measures. The signal is 14.6 seconds long and has a sampling frequency  $f_s = 44100\text{Hz}$  yielding  $T = 643817$  samples.



Fig. 2: Musical score of the second audio sample (referred as dataset 2).

The music samples have been generated with a professional audio software called Sibelius based on the musical score shown in Figures 1 and 2.

2) *Experimental comparison*: This section describes the test procedure elaborated to evaluate the quality of the results obtained with MR- $\beta$ -NMF (6) that jointly factorizes two audio spectrograms  $X$  and  $Y$ . In the following, matrices  $W$  and  $H$  stand for the solutions computed with Algorithm 1 that solves MR- $\beta$ -NMF (6). We aim at showing that the factor  $W$  has a high frequency resolution whereas the matrix  $H$  has a high temporal resolution. To achieve this goal, we compare  $W$  to a dictionary matrix denoted  $W_Y$  computed with a baseline  $\beta$ -NMF approach that factorizes the high frequency

spectrogram  $Y$  only. The baseline  $\beta$ -NMF applied on  $Y$  solves the following optimization problem:

$$\min_{W_Y \geq 0, H_Y \geq 0} D_\beta(Y|W_Y H_Y). \quad (14)$$

Due to the trade-off between detailed frequency and temporal information, the activation matrix  $H_Y$  shows a low temporal resolution. To compare the accuracy of the solutions  $W$  and  $W_Y$ , we need to have access to an oracle matrix  $W_\#$  that is the reference for the comparison. For instance, for the dataset 1, each column of  $W_\#$  is supposedly the “true” spectral signature of each of the three notes;  $E_4$ ,  $D_4$  and  $C_4$ . We estimated  $W_\#$  as follows:

- We synthetically generate three audio signals and each one contains the sequence of one note in particular.
- Based on the three audio signals, we generate three amplitude spectrograms that have high frequency resolution with the same window size as the one used to generate  $Y$ .
- For each amplitude spectrogram, we perform a rank-1 NMF. The resulting  $F_Y$ -dimensional vectors are concatenated to form the oracle matrix  $W_\#$ .

We show the accuracy of  $H$  with a similar procedure;  $H$  is compared to an activation matrix  $H_X$  obtained by solving

$$\min_{W_X \geq 0, H_X \geq 0} D_\beta(X|W_X H_X), \quad (15)$$

using multiplicative updates. The oracle matrix  $H_\#$ , that is, the reference for the comparison, is computed by performing three independent rank-1 NMF on three amplitude spectrograms that have high temporal resolution, all generated with the same window size as the one used to generate  $X$ .

3) *Performance Evaluation*: This section presents the qualitative criteria for evaluating the performance of the solutions obtained with Algorithm 1. We compute the following measures of reconstruction.

- *Activation matrices*: in order to avoid the scaling and permutation ambiguities inherent to the considered NMF models, we first normalize in L-1 norm the rows of the activations matrices  $H$  and solve an assignment problem w.r.t. the oracle matrix  $H_\#$ . The quality of the activation matrix  $H$  is compared to  $H_X$  w.r.t.  $H_\#$  by computing the following signal-to-noise ratios (SNR): for all  $k$ ,

$$SNR_{H_k} = 20 \log_{10} \left( \frac{\|\bar{H}(k, :)\|_F}{\|\bar{H}(k, :) - \bar{H}_\#(k, :)\|_F} \right), \quad (16)$$



where  $\bar{H}(k, :) = \frac{H(k, :)}{\|H(k, :)\|_1}$  and  $\|H(k, :)\|_1 = \sum_j |H(k, j)|$ , and

$$SNR_{H_X, k} = 20 \log_{10} \left( \frac{\|\bar{H}_X(k, :)\|_F}{\|\bar{H}_X(k, :) - \bar{H}_\#(k, :)\|_F} \right). \quad (17)$$

The higher the SNRs (16) and (17), the better is the estimation for the activation matrix.

• *Dictionary matrices*: The quality of the dictionary matrix  $W$  is evaluated in the same fashion, except that the normalization is performed by columns.

## B. Results

In this section, we use the following setting:

- 100 random initializations for  $W$  and  $H$  for each NMF.
- the window lengths are set to 1024 (23ms) and 4096 (93ms), then the downsampling ratio  $d$  is equal to 4. For the generation of  $R$  and  $S$ , parameter  $f$  is set to 2.
- $\beta = 1$ , and we consider the amplitude spectrograms as the input data.
- we use  $\lambda = 1$  in all our experiments.

1) *Dataset 1: "Mary had a little lamb"*: In this section we report the numerical results obtained after the completion of the test set up presented in section IV-A, and using MAXITERL1=100 and MAXITERL2=400. for Algorithm 1.

Table II reports the average SNR, the standard deviation and the best SNR computed for the activations and dictionary vectors obtained with the models described in Section IV-A2 over the 100 initializations. As it can be observed, activations  $H$  are slightly better than activations  $H_X$ , and with a significant lower standard deviation for each note. The results for the dictionary are even more conclusive; MR- $\beta$ -NMF outperforms baseline NMF (14) for which the SNR (best case) can be up to two times larger. Moreover, the standard deviations of MR- $\beta$ -NMF are significantly lower than those obtained with baseline NMF (14). It appears that the second term in the objective function in (6) acts as a regularizer so that MR- $\beta$ -NMF is more robust to different initializations.

Figure 3 shows the dictionary matrices  $W_\#$ ,  $W$ ,  $W_Y$  and  $W_X$ . For more clarity, the frequency range is limited to 2 kHz. This limited range includes all the most significant peaks in terms of magnitude. We observe that all the frequency peaks are accurately estimated by MR- $\beta$ -NMF for each note. Figure 3 also integrates the dictionary matrix  $W_X$  to highlight the impact of using baseline NMF (15) that uses a higher temporal resolution.

We conclude that MR- $\beta$ -NMF is able to obtain more robust and more accurate results than baseline  $\beta$ -NMFs that factorize a single spectrogram.

2) *Dataset 2*: In this section we report the numerical results obtained for dataset 2, using MAXITERL1=500 and MAXITERL2=1500 for Algorithm 1.

Table III reports the average SNR, the standard deviation and the best SNR computed for activations and dictionary vectors obtained with the methods described in IV-A2 over 100 initializations. We observe that:

- MR- $\beta$ -NMF provides results that show high resolutions in both frequency and temporal domains,

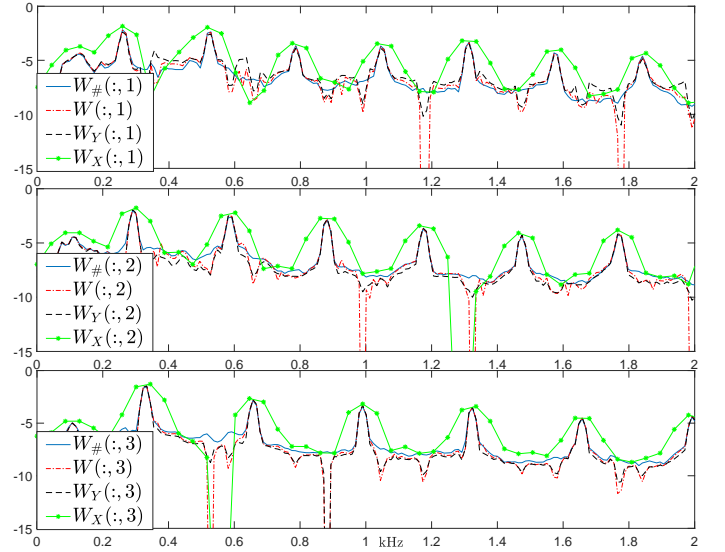


Fig. 3: Columns of  $W_\#$ ,  $W$ ,  $W_Y$  and  $W_X$  in semi-log scale. Top, middle and bottom sub-figures show the spectral content respectively for  $C_4$ ,  $D_4$  and  $E_4$ .

- the regularization effect of MR- $\beta$ -NMF w.r.t. baseline NMFs is less stunning than observed for dataset 1. However the standard deviations obtained with MR- $\beta$ -NMF for the dictionary are significantly lower than those obtained with the baseline NMFs.
- by looking more accurately at the results for the dictionary, MR- $\beta$ -NMF globally performs better than baseline NMFs. For the activations, baseline NMFs perform slightly better than MR- $\beta$ -NMF for three scores, with an improvement of at most 1.9% (for the  $F_4$  score).

## V. NUMERICAL EXPERIMENTS ON HS-MS FUSION

In this section, we perform numerical experiments to validate the effectiveness of MR- $\beta$ -NMF on the HS-MS fusion problem.

### A. Test setup and criteria

1) *Test data*: The proposed MR- $\beta$ -NMF algorithm is tested on semi-real datasets against several methods and algorithms widely used to tackle the HS-MS data fusion problem, namely GSA [28], CNMF [10], HySure [29], FUMI [30], GLP [31], MAPSMM [32], SFIM [33] and Lanaras's method [34]. In a nutshell: GSA, SFIM and GLP are pansharpening-based methods, the remaining methods belong to subspace-based methods that can be splitted into unmixing methods (CNMF, Lanaras's method and HySure) and Bayesian-based approaches (FUMI, MAPSMM) [23].

All the algorithms are implemented and tested on a desktop computer with Intel Core i7-8700@3.2GHz CPU, Geforce RTX 2070 Super GPU and 32GB memory. The codes<sup>1</sup> are written in MATLAB R2018a. The implementation for benchmarked algorithms comes from the comparative review of the

<sup>1</sup><https://naotoyokoya.com/Download.html>

TABLE II: Comparison of MR- $\beta$ -NMF with baseline  $\beta$ -NMF in terms of SNR on the activations and the dictionary vectors with respect to true factors on the dataset 1. The table reports the average, standard deviation and the best SNR over 100 random initializations for  $W$  and  $H$ . Bold numbers indicate the highest SNR.

Note	Activation SNR's (dB)				Basis SNR's (dB)			
	$SNR_{H_k}$		$SNR_{H_{X,k}}$		$SNR_{W_k}$		$SNR_{W_{Y,k}}$	
	average $\pm$ std	best	average $\pm$ std	best	average $\pm$ std	best	average $\pm$ std	best
$C_4$	12.33 $\pm$ 0.17	<b>12.74</b>	3.89 $\pm$ 8.99	12.19	21.35 $\pm$ 1.77	<b>22.66</b>	7.95 $\pm$ 7.84	12.38
$D_4$	14.50 $\pm$ 0.08	<b>14.62</b>	8.57 $\pm$ 6.44	14.38	21.25 $\pm$ 0.35	<b>21.61</b>	14.71 $\pm$ 6.06	18.23
$E_4$	19.68 $\pm$ 0.04	<b>19.82</b>	15.28 $\pm$ 5.06	19.74	22.71 $\pm$ 0.36	<b>23.02</b>	19.36 $\pm$ 2.02	20.66

TABLE III: Comparison of MR- $\beta$ -NMF with baseline  $\beta$ -NMF in terms of SNR on the activations and the dictionary vectors with respect to true factors on the dataset 2. The table reports the average, standard deviation and the best SNR over 100 random initializations for  $W$  and  $H$ . Bold numbers indicate the highest SNR.

Note	Activation SNR's (dB)				dictionary SNR's (dB)			
	$SNR_{H_k}$		$SNR_{H_{X,k}}$		$SNR_{W_k}$		$SNR_{W_{Y,k}}$	
	average $\pm$ std	best	average $\pm$ std	best	average $\pm$ std	best	average $\pm$ std	best
$A_4$	11.98 $\pm$ 0.01	12.03	12.17 $\pm$ 0.01	<b>12.17</b>	16.24 $\pm$ 0.02	<b>16.43</b>	16.29 $\pm$ 0.26	16.42
$C_5$	9.54 $\pm$ 0.02	<b>9.57</b>	9.43 $\pm$ 0.01	9.43	9.41 $\pm$ 0.02	<b>9.42</b>	8.61 $\pm$ 0.72	8.73
$D_4$	14.81 $\pm$ 0.01	14.82	14.92 $\pm$ 0.01	<b>14.92</b>	16.20 $\pm$ 0.06	<b>16.33</b>	15.24 $\pm$ 2.37	15.64
$F_4$	11.23 $\pm$ 0.01	11.32	11.52 $\pm$ 0.01	<b>11.54</b>	16.47 $\pm$ 0.05	16.50	16.76 $\pm$ 0.99	<b>16.93</b>

recent literature for HS and MS data fusion detailed in [23]. We consider the following real HS datasets:

- HYDICE Urban: The Urban dataset<sup>2</sup> consists of  $307 \times 307$  pixels and 162 spectral reflectance bands in the wavelength range 400 nm to 2500 nm. We extract a  $120 \times 120$  subimage from this dataset.
- HYDICE Washington DC Mall: this dataset<sup>3</sup> has been acquired with HYDICE HS sensor over the Washington DC Mall and consists of  $1208 \times 307$  pixels and 191 spectral reflectance bands in the wavelength range 400 nm to 2500 nm. We extract a  $240 \times 240$  subimage from this dataset.
- AVIRIS Indian Pines: this dataset has been acquired with NASA Airborne Visible/Infrared Imaging (AVIRIS) Spectrometer [35] over the Indian Pines test site in North-western Indiana and consists of  $145 \times 145$  pixels and 200 spectral reflectance bands in the wavelength range 400 nm to 2500 nm. We extract a  $120 \times 120$  subimage from this dataset.

Note that entries of the datasets are uncalibrated relative values, also referred as Digital Numbers (DN). As the goal is to fuse data and not to perform HS unmixing and classification, we do not convert these values into reflectances.

2) *Test procedure:* In this paper we consider semi-real data by conducting the numerical experiments based on the widely used Wald's protocol [36]. This protocol consists in simulating input MS and HS images from a reference high-resolution HS image. In this paper, MS image  $X$  and HS image  $Y$  have been derived from high-resolution HS image  $V$  through the models (4) and (5) respectively. Let us recall that the operator  $R$  from (1) designates the relative spectral responses from the super-resolution image to the MS image. In other words, it defines how the satellite instruments measure the intensity of the wavelengths (colors) of light. We generate a six-band MS image  $X$  by filtering the reference image  $V$  with the Landsat 4 TM-like reflectance spectral responses<sup>4</sup>. The Landsat 4 TM

sensor [37] has a spectral coverage from 400 nm to 2500 nm so that it is consistent with the spectral coverage of the datasets.

The operator  $S$  (5) corresponds to the process of spatial blurring and downsampling. The high spectral low spatial resolution HS image  $Y$  is generated by applying a  $11 \times 11$  Gaussian spatial filter with a standard deviation of 1.7 on each band of the reference image  $V$  and downsampling every 4 pixels, both horizontally and vertically. The HS and MS images are finally both contaminated with noise. The level of noise is usually characterized by the SNR expressed in dB. Here,  $SNR_X$  and  $SNR_Y$  refer to the noise level for the MS and HS images respectively. In this paper, we apply the same level of noise for each spectral band. Let us give more insights on the last step of the MS image generation:  $X = \max(0, RV + \epsilon_X)$  where the noise matrix  $\epsilon_X$  is constructed as follows: we introduce  $x_i$  for  $i = 1, 2$ , some binary coefficients, and

$$\tilde{N} = x_1 \frac{N_P}{\|N_P\|_F} + x_2 \frac{N_F}{\|N_F\|_F},$$

where

- Each entry of  $N_P$  is generated using the Poisson distribution of parameter  $(R\tilde{V})_{i,j}$  for all  $(i, j)$ , where  $\tilde{V}$  is a noiseless low-rank approximation of  $V$  that is computed separately. More precisely, by setting  $\epsilon_X = 0_{F_X \times N_X}$  where  $0_{F_X \times N_X}$  is all-zero matrix, a solution  $(W, H)$  for MR- $\beta$ -NMF (6) is first computed with Algorithm 1, and the parameter for the Poisson distribution is defined as  $\tilde{V} = WH$ .

- Each entry of  $N_F$  is generated using the normal distribution of mean 0 and variance 1.

We set  $\epsilon_X = \eta \frac{\|RV\|_F}{\|\tilde{N}\|_F} \tilde{N}$  with  $\eta = \frac{1}{10^{-20} SNR_X}$ . For example, if we fix  $SNR_X = 25dB$ ,  $V_1 = \max(0, RV + \epsilon_X)$  is a MS image contaminated with 5.62% of noise (that is,  $\|\epsilon_X\|_F = 0.0562\|RV\|_F$ ) and projected onto the nonnegative orthant. The noise matrix  $\epsilon_Y$  is obtained in the same way.

The benchmarked algorithms listed in V-A1 are configured as recommended in the comparative review [23] with the following variations:

<sup>2</sup><http://lesun.weebly.com/hyperspectral-data-set.html>

<sup>3</sup><https://engineering.purdue.edu/~biehl/MultiSpec/hyperspectral.html>

<sup>4</sup><https://landsat.usgs.gov/spectral-characteristics-viewer>



- The number of endmembers is a key parameter for unmixing-based methods. For MR- $\beta$ -NMF, CNMF, Lanaras's method and HySure,  $K$  is set to the 5 and 6 for HYDICE Urban and HYDICE Washington DC Mall datasets respectively as done in [38]. For the Indian Pine dataset,  $K = 16$  as in [39].
- The benchmarked algorithms are stopped when the relative change of the objective function is below  $10^{-4}$  or when the number of iterations exceeds 500. For algorithms such as CNMF that include outer and inner loops, we contacted the authors to set up the best balance for the maximum number of inner ( $I_1$ ) and outer ( $I_2$ ) loop iterations to fairly compare the methods, the following couples of values are considered:  $I_1 = 100$  and  $I_2 = 5$  and  $I_1 = 250$  and  $I_2 = 2$ . The couple of values that gives the best results for each dataset is considered in section V-B, that is  $I_1 = 100$  and  $I_2 = 5$ .
- The matrix  $R$  is known for all algorithms that make use of it. For MR- $\beta$ -NMF, it means we use MAXITERL1=500 and MAXITERL2=0.

Finally, let us summarize the initialization strategy:

- MR- $\beta$ -NMF uses random nonnegative initializations for  $W$  and  $H$ .
- CNMF starts by unmixing the HS image using VCA [40] to initialize the endmember signatures,
- SISAL [41] is used to initialize the endmembers for Lanaras's method.

Four variants of the MR- $\beta$ -NMF are considered, namely  $\beta = 2$ ,  $\beta = \frac{3}{2}$ ,  $\beta = 1$  and  $\beta = \frac{1}{2}$ . We test the algorithms under a scenario where no noise is added (that is,  $\tilde{N} = 0$ ), and a scenario where noise is added so that the SNRs for the noise terms in  $\epsilon_X$  and  $\epsilon_Y$  are  $SNR_X = 25dB$  and  $SNR_Y = 25dB$ .

3) *Performance evaluation*: In order to assess the fusion quantitatively, we use the following five complementary and widely used quality measurements:

- Peak SNR (PSNR): the PSNR is used to assess the spatial reconstruction quality of each band. It corresponds to the ratio between the maximum power of a signal and the power of residual errors. A larger PSNR value indicates a higher quality of spatial reconstruction.
- The root-mean-square error (RMSE): RMSE is a similarity measure between the super-resolution image  $V$  and the fused image  $\hat{V} = WH$ . The smaller the RMSE is, the better the fusion quality is.
- Erreur Relative Globale Adimensionnelle de Synthèse (ERGAS): ERGAS provides a macroscopic statistical measure of the quality of the fused data. More precisely, ERGAS calculates the amount of spectral distortion in the image [42]. The best value is at 0.
- Spectral Angle Mapper (SAM): SAM is used to quantify the spectral information preservation at each pixel. More precisely, SAM determines the spectral distance by computing the angle between two vectors of the estimated and reference spectra. The overall SAM is obtained by averaging the SAMs computed for all image pixels. The smaller the absolute value of SAM is, the better the fusion quality is.
- The universal image quality index (UIQI) introduced in [43]: UIQI evaluates the similarity between two single-band images. It is related to the correlation, luminance distortion, and contrast distortion of the estimated image w.r.t. reference

image. UIQI indicator is in the range  $[-1, 1]$ . For multiband images, the overall UIQI is computed by averaging the UIQI computed band by band. The best value for UIQI is at 1.

For more details about these quality measurements, we refer the reader to [44] and [30].

## B. EXPERIMENTAL RESULTS

We ran 20 independent trials for each dataset detailed in V-A1. The average performance of each algorithm is shown in Tables IV to VI. Except for runtimes, MR- $\beta$ -NMF generally rank in the fifth first for all the quality measurements. For Urban dataset with noise added, MR- $\beta$ -NMF with  $\beta = 1$ ,  $\beta = 1/2$  and  $\beta = 3/2$  respectively rank first, second and third for all the metrics except for SAM for which CNMF ranks first. For the condition with no noise added, MR- $\beta$ -NMF with  $\beta = 1$ ,  $\beta = 1/2$  ranks first and second for all metrics. MR- $\beta$ -NMF with  $\beta = 3/2$ , FUMI and HySure give similar results. For Washington DC Mall without noise added, MR- $\beta$ -NMF with  $\beta = 1$ ,  $\beta = 1/2$  ranks first and second for all metrics. For Indian Pines dataset without noise added, MR- $\beta$ -NMF with  $\beta = 1$  ranks second while HySure ranks first. When noise is added, Lanaras's method ranks first while MR- $\beta$ -NMF with  $\beta = 1/2$ ,  $\beta = 1$  rank second and third for most criteria. In order to give more insights on the performance comparison between algorithms, Figure 4 displays the SAM maps obtained for one trial for the Urban, Washington DC Mall and Indian Pines datasets. Visually, the proposed method performs competitively with other state-of-the-art methods. Indeed, as already observed with the SAM comparison in Tables IV to VI, the variants of MR- $\beta$ -NMF show in general lower values for SAM errors across the images. For the Urban dataset, the highest SAM errors obtained with the variants of MR- $\beta$ -NMF are less widespread and localized at some specific spots which correspond to the edges of the roofs and trees. This observation makes sense as those regions show more atypical reflectance angles and therefore more non-linear effects in terms of spectral mixture. The same observations apply for the Washington DC Mall dataset with and without noise added. For the Indian Pines dataset without noise added, HySure and FUMI algorithms show lower SAM errors across images, we visually confirm that MR- $\beta$ -NMF with  $\beta = 1, 1/2, 3/2$  rank third to fifth. When the noise is added, Lanaras's method gives the lowest SAM errors and is less widespread, while MR- $\beta$ -NMF with  $\beta = 1, 1/2, 3/2$  appear to provide less accurate estimates than CNMF that visually looks better.

## VI. CONCLUSIONS AND OUTLOOKS

In this paper, we have presented a new NMF approach for blind spectral unmixing, called multi-resolution  $\beta$ -NMF (MR- $\beta$ -NMF). The estimation relies on the minimization of the  $\beta$ -divergence, a flexible family of measures of fit. MR- $\beta$ -NMF addresses the resolution trade-off between two adversarial dimensions by fusing the information coming from multiple data with different resolutions in order to produce a factorization with high resolutions for all the dimensions. We have provided

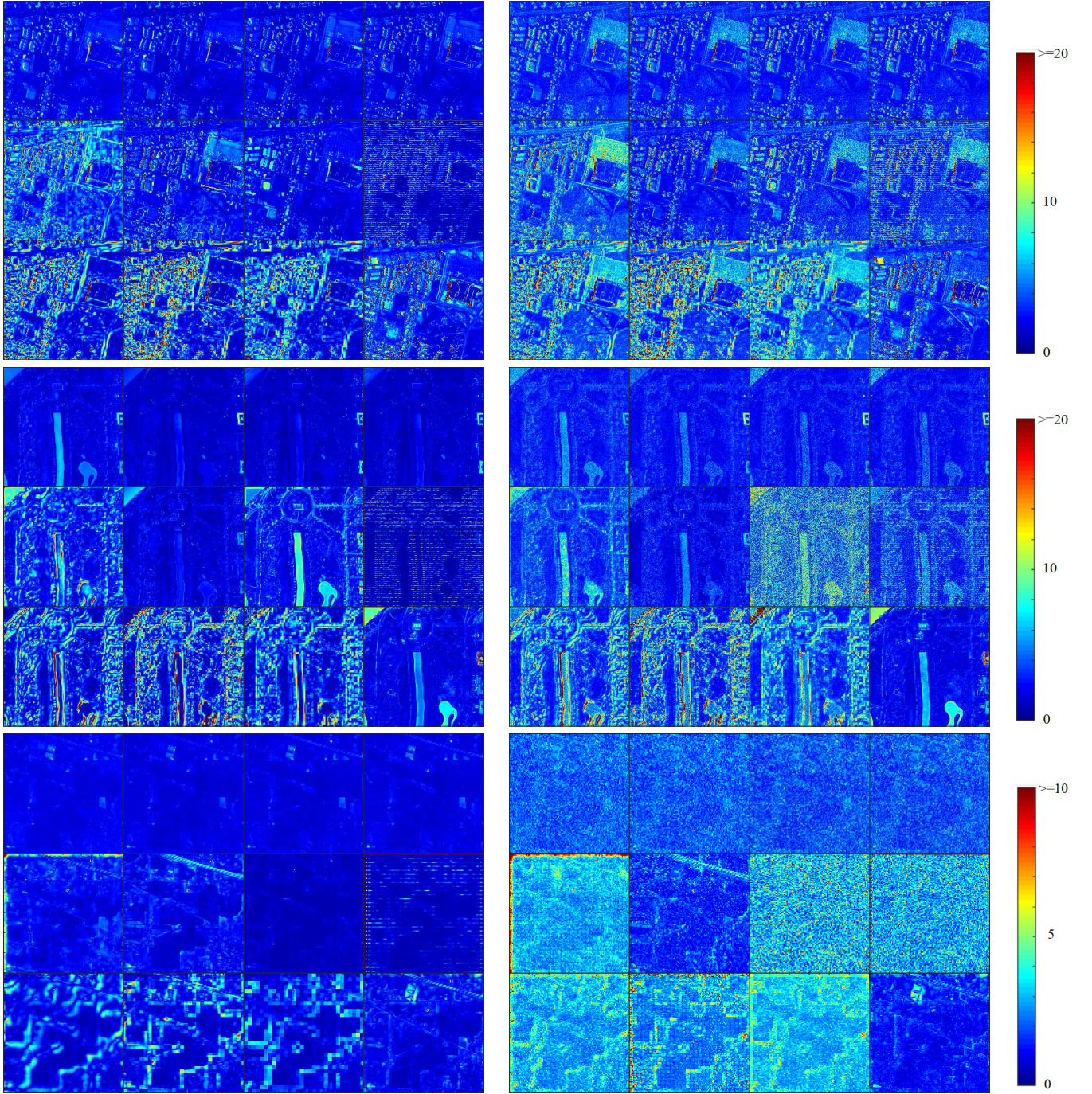


Fig. 4: SAM maps for the different hyperspectral images. From top to bottom: Urban dataset with  $K = 5$ , Washington DC Mall dataset with  $K = 6$ , and Indian Pines dataset with  $K = 16$ . On the left column: SAM maps without added noise. On the right column: SAM maps with added noise ( $SNR_X = SNR_Y = 25dB$ ). For each image, the 12 SAM maps correspond to the different benchmark algorithms; from left to right, top to bottom: MR-2-NMF, MR-3/2-NMF, MR-1-NMF, MR-1/2-NMF, GSA, CNMF, HySure, FUMI, GLP, MAPSMM, SFIM, and Lanaras's method.



TABLE IV: Comparison of MR- $\beta$ -NMF with state-of-the-arts methods for HS-MS fusion problem on dataset HYDICE Urban. The table reports the average, standard deviation for the quantitative quality assessments over 20 trials. Bold, underlined and italic to highlight the three best algorithms.

Method	Runtime (seconds)	PSNR (dB)	RMSE	ERGAS	SAM	UIQI
Best value	0	$\infty$	0	0	0	1
Dataset - HYDICE Urban - $SNR = 25dB$						
MR- $\beta = 2$ -NMF	52.25 $\pm$ 2.45	33.88 $\pm$ 0.10	16.26 $\pm$ 0.19	2.48 $\pm$ 0.03	4.13 $\pm$ 0.06	0.97 $\pm$ 0.00
MR- $\beta = 3/2$ -NMF	54.46 $\pm$ 2.31	<u>34.54 <math>\pm</math> 0.06</u>	<u>14.92 <math>\pm</math> 0.09</u>	2.28 $\pm$ 0.01	3.65 $\pm$ 0.04	<u>0.98 <math>\pm</math> 0.00</u>
MR- $\beta = 1$ -NMF	52.20 $\pm$ 2.03	<b>34.85 <math>\pm</math> 0.10</b>	<b>14.51 <math>\pm</math> 0.14</b>	<b>2.22 <math>\pm</math> 0.03</b>	<b>3.49 <math>\pm</math> 0.06</b>	<b>0.98 <math>\pm</math> 0.00</b>
MR- $\beta = 1/2$ -NMF	54.47 $\pm$ 1.96	34.81 $\pm$ 0.10	14.65 $\pm$ 0.15	2.24 $\pm$ 0.02	3.52 $\pm$ 0.06	0.98 $\pm$ 0.00
GSA	0.72 $\pm$ 0.05	32.52 $\pm$ 0.00	19.41 $\pm$ 0.00	2.87 $\pm$ 0.00	5.63 $\pm$ 0.00	0.96 $\pm$ 0.00
CNMF	9.73 $\pm$ 1.84	34.33 $\pm$ 0.50	15.45 $\pm$ 0.85	2.37 $\pm$ 0.17	3.64 $\pm$ 0.27	0.98 $\pm$ 0.00
HySure	31.57 $\pm$ 2.93	33.90 $\pm$ 0.00	16.44 $\pm$ 0.00	2.57 $\pm$ 0.00	4.17 $\pm$ 0.00	0.97 $\pm$ 0.00
FUMI	0.39 $\pm$ 0.03	32.92 $\pm$ 0.00	20.30 $\pm$ 0.00	2.85 $\pm$ 0.00	4.92 $\pm$ 0.00	0.96 $\pm$ 0.00
GLP	6.05 $\pm$ 0.42	27.24 $\pm$ 0.00	34.37 $\pm$ 0.00	5.10 $\pm$ 0.00	6.27 $\pm$ 0.00	0.91 $\pm$ 0.00
MAPSMM	44.12 $\pm$ 2.60	25.57 $\pm$ 0.00	41.95 $\pm$ 0.00	6.15 $\pm$ 0.00	6.82 $\pm$ 0.00	0.87 $\pm$ 0.00
SFIM	<b>0.24 <math>\pm</math> 0.03</b>	26.32 $\pm$ 0.00	37.89 $\pm$ 0.00	5.71 $\pm$ 0.00	5.90 $\pm$ 0.00	0.90 $\pm$ 0.00
Lanaras's method	8.12 $\pm$ 8.71	29.33 $\pm$ 0.29	26.84 $\pm$ 0.85	4.39 $\pm$ 0.23	4.88 $\pm$ 0.26	0.94 $\pm$ 0.00
Dataset - HYDICE Urban - No added noise						
MR- $\beta = 2$ -NMF	49.55 $\pm$ 0.31	38.10 $\pm$ 0.40	10.94 $\pm$ 0.31	1.67 $\pm$ 0.07	3.28 $\pm$ 0.10	0.99 $\pm$ 0.00
MR- $\beta = 3/2$ -NMF	51.54 $\pm$ 0.52	40.01 $\pm$ 0.50	8.82 $\pm$ 0.32	<u>1.35 <math>\pm</math> 0.09</u>	2.60 $\pm$ 0.10	<u>0.99 <math>\pm</math> 0.00</u>
MR- $\beta = 1$ -NMF	49.71 $\pm$ 0.12	41.53 $\pm$ 0.56	7.86 $\pm$ 0.28	<b>1.19 <math>\pm</math> 0.07</b>	2.27 $\pm$ 0.10	<b>0.99 <math>\pm</math> 0.00</b>
MR- $\beta = 1/2$ -NMF	52.09 $\pm$ 0.35	<u>41.69 <math>\pm</math> 0.64</u>	<b>7.81 <math>\pm</math> 0.35</b>	1.19 $\pm$ 0.08	<b>2.23 <math>\pm</math> 0.12</b>	0.99 $\pm$ 0.00
GSA	0.67 $\pm$ 0.04	32.93 $\pm$ 0.00	22.17 $\pm$ 0.00	2.87 $\pm$ 0.00	5.25 $\pm$ 0.00	0.97 $\pm$ 0.00
CNMF	10.56 $\pm$ 2.02	35.35 $\pm$ 0.64	13.91 $\pm$ 1.81	2.18 $\pm$ 0.32	3.26 $\pm$ 0.53	0.98 $\pm$ 0.00
HySure	28.51 $\pm$ 1.09	40.27 $\pm$ 0.00	9.67 $\pm$ 0.00	1.46 $\pm$ 0.00	2.50 $\pm$ 0.00	0.99 $\pm$ 0.00
FUMI	0.36 $\pm$ 0.02	41.01 $\pm$ 0.00	14.14 $\pm$ 0.00	1.67 $\pm$ 0.00	2.71 $\pm$ 0.00	0.99 $\pm$ 0.00
GLP	5.61 $\pm$ 0.09	27.97 $\pm$ 0.00	31.97 $\pm$ 0.00	4.65 $\pm$ 0.00	4.78 $\pm$ 0.00	0.94 $\pm$ 0.00
MAPSMM	42.19 $\pm$ 0.84	25.92 $\pm$ 0.00	40.56 $\pm$ 0.00	5.89 $\pm$ 0.00	5.66 $\pm$ 0.00	0.89 $\pm$ 0.00
SFIM	<b>0.21 <math>\pm</math> 0.03</b>	27.05 $\pm$ 0.00	35.19 $\pm$ 0.00	5.21 $\pm$ 0.00	4.21 $\pm$ 0.00	0.93 $\pm$ 0.00
Lanaras's method	4.72 $\pm$ 4.72	29.50 $\pm$ 0.35	26.54 $\pm$ 0.69	4.26 $\pm$ 0.23	4.57 $\pm$ 0.21	0.95 $\pm$ 0.00

TABLE V: Comparison of MR- $\beta$ -NMF with state-of-the-arts methods for HS-MS fusion problem on dataset HYDICE Washington DC Mall. The table reports the average, standard deviation for the quantitative quality assessments over 20 trials. Bold, underlined and italic to highlight the three best algorithms.

Method	Runtime (seconds)	PSNR (dB)	RMSE	ERGAS	SAM	UIQI
Best value	0	$\infty$	0	0	0	1
Dataset - HYDICE Washington DC Mall - $SNR = 25dB$						
MR- $\beta = 2$ -NMF	57.59 $\pm$ 0.32	26.77 $\pm$ 0.25	202.02 $\pm$ 3.59	18.21 $\pm$ 0.13	3.38 $\pm$ 0.11	<b>0.90 <math>\pm</math> 0.01</b>
MR- $\beta = 3/2$ -NMF	60.04 $\pm$ 0.39	<u>26.37 <math>\pm</math> 0.32</u>	<u>194.40 <math>\pm</math> 6.38</u>	<u>18.07 <math>\pm</math> 0.23</u>	3.05 $\pm$ 0.18	0.87 $\pm$ 0.01
MR- $\beta = 1$ -NMF	57.95 $\pm$ 0.24	26.29 $\pm$ 0.20	<b>188.42 <math>\pm</math> 11.18</b>	18.50 $\pm$ 0.25	2.83 $\pm$ 0.28	0.86 $\pm$ 0.01
MR- $\beta = 1/2$ -NMF	60.38 $\pm$ 0.20	25.68 $\pm$ 0.28	201.62 $\pm$ 14.05	19.46 $\pm$ 0.41	3.06 $\pm$ 0.30	0.83 $\pm$ 0.01
GSA	0.79 $\pm$ 0.04	23.00 $\pm$ 0.00	235.64 $\pm$ 0.00	32.25 $\pm$ 0.00	4.20 $\pm$ 0.00	0.74 $\pm$ 0.00
CNMF	7.25 $\pm$ 1.26	<b>27.60 <math>\pm</math> 0.09</b>	<u>192.67 <math>\pm</math> 6.50</u>	<u>17.37 <math>\pm</math> 0.10</u>	<b>2.55 <math>\pm</math> 0.14</b>	0.89 $\pm$ 0.00
HySure	34.14 $\pm$ 0.94	24.01 $\pm$ 0.00	351.13 $\pm$ 0.00	33.51 $\pm$ 0.00	6.15 $\pm$ 0.00	0.75 $\pm$ 0.00
FUMI	0.42 $\pm$ 0.02	24.67 $\pm$ 0.00	243.06 $\pm$ 0.00	19.73 $\pm$ 0.00	4.04 $\pm$ 0.00	0.80 $\pm$ 0.00
GLP	6.42 $\pm$ 0.24	19.85 $\pm$ 0.00	423.89 $\pm$ 0.00	33.64 $\pm$ 0.00	5.28 $\pm$ 0.00	0.67 $\pm$ 0.00
MAPSMM	40.91 $\pm$ 0.46	19.34 $\pm$ 0.00	494.39 $\pm$ 0.00	32.18 $\pm$ 0.00	5.91 $\pm$ 0.00	0.65 $\pm$ 0.00
SFIM	<b>0.24 <math>\pm</math> 0.01</b>	18.08 $\pm$ 0.00	892.35 $\pm$ 0.00	<u>42.23 <math>\pm</math> 0.00</u>	5.45 $\pm$ 0.00	0.64 $\pm$ 0.00
Lanaras's method	3.11 $\pm$ 1.94	25.95 $\pm$ 0.06	235.62 $\pm$ 2.67	<b>17.36 <math>\pm</math> 0.02</b>	2.78 $\pm$ 0.03	0.90 $\pm$ 0.00
Dataset - HYDICE Washington DC Mall - No added noise						
MR- $\beta = 2$ -NMF	58.55 $\pm$ 1.50	32.61 $\pm$ 0.28	128.50 $\pm$ 5.87	5.54 $\pm$ 0.13	2.59 $\pm$ 0.12	0.97 $\pm$ 0.00
MR- $\beta = 3/2$ -NMF	60.95 $\pm$ 1.58	35.36 $\pm$ 0.38	<u>104.11 <math>\pm</math> 5.89</u>	2.41 $\pm$ 0.22	1.89 $\pm$ 0.12	<u>0.98 <math>\pm</math> 0.00</u>
MR- $\beta = 1$ -NMF	59.01 $\pm$ 2.02	<u>37.80 <math>\pm</math> 0.75</u>	<b>89.20 <math>\pm</math> 5.43</b>	<u>1.76 <math>\pm</math> 0.27</u>	<b>1.47 <math>\pm</math> 0.07</b>	<b>0.99 <math>\pm</math> 0.00</b>
MR- $\beta = 1/2$ -NMF	61.21 $\pm$ 1.05	<b>38.27 <math>\pm</math> 0.83</b>	90.88 $\pm$ 6.26	<b>1.55 <math>\pm</math> 0.20</b>	1.48 $\pm$ 0.10	0.99 $\pm$ 0.00
GSA	0.81 $\pm$ 0.08	29.93 $\pm$ 0.00	262.27 $\pm$ 0.00	3.11 $\pm$ 0.00	3.84 $\pm$ 0.00	0.97 $\pm$ 0.00
CNMF	7.90 $\pm$ 2.67	31.46 $\pm$ 1.07	152.95 $\pm$ 14.25	5.93 $\pm$ 8.92	2.01 $\pm$ 0.49	0.96 $\pm$ 0.03
HySure	35.85 $\pm$ 2.19	31.23 $\pm$ 0.00	190.57 $\pm$ 0.10	3.21 $\pm$ 0.00	3.21 $\pm$ 0.00	0.96 $\pm$ 0.00
FUMI	0.43 $\pm$ 0.03	36.52 $\pm$ 0.00	142.92 $\pm$ 0.00	2.32 $\pm$ 0.00	<u>1.76 <math>\pm</math> 0.00</u>	0.98 $\pm$ 0.00
GLP	6.95 $\pm$ 0.52	26.19 $\pm$ 0.00	373.07 $\pm$ 0.00	4.53 $\pm$ 0.00	4.16 $\pm$ 0.00	0.93 $\pm$ 0.00
MAPSMM	42.88 $\pm$ 0.85	24.42 $\pm$ 0.00	459.09 $\pm$ 0.00	5.61 $\pm$ 0.00	4.98 $\pm$ 0.00	0.88 $\pm$ 0.00
SFIM	<b>0.27 <math>\pm</math> 0.05</b>	25.12 $\pm$ 0.00	408.40 $\pm$ 0.00	6.53 $\pm$ 0.00	3.95 $\pm$ 0.00	0.92 $\pm$ 0.00
Lanaras's method	4.70 $\pm$ 3.55	28.46 $\pm$ 0.36	230.31 $\pm$ 7.44	3.94 $\pm$ 0.21	2.55 $\pm$ 0.03	0.96 $\pm$ 0.00

TABLE VI: Comparison of MR- $\beta$ -NMF with state-of-the-arts methods for HS-MS fusion problem on dataset AVIRIS Indian Pines. The table reports the average, standard deviation for the quantitative quality assessments over 20 trials. Bold, underlined and italic to highlight the three best algorithms.

Method	Runtime (seconds)	PSNR (dB)	RMSE	ERGAS	SAM	UIQI
Best value	0	$\infty$	0	0	0	1
Dataset - AVIRIS Indian Pines - $SNR = 25dB$						
MR- $\beta = 2$ -NMF	15.48 $\pm$ 0.53	27.11 $\pm$ 0.03	187.37 $\pm$ 0.80	1.64 $\pm$ 0.01	2.26 $\pm$ 0.02	0.78 $\pm$ 0.00
MR- $\beta = 3/2$ -NMF	16.76 $\pm$ 0.75	27.29 $\pm$ 0.02	183.47 $\pm$ 0.56	1.57 $\pm$ 0.00	2.14 $\pm$ 0.01	0.78 $\pm$ 0.00
MR- $\beta = 1$ -NMF	15.57 $\pm$ 0.53	27.38 $\pm$ 0.02	181.77 $\pm$ 0.51	1.55 $\pm$ 0.00	2.09 $\pm$ 0.01	0.78 $\pm$ 0.00
MR- $\beta = 1/2$ -NMF	16.90 $\pm$ 0.55	27.55 $\pm$ 0.03	179.10 $\pm$ 0.41	1.52 $\pm$ 0.01	2.03 $\pm$ 0.01	<b>0.79 <math>\pm</math> 0.00</b>
GSA	0.31 $\pm$ 0.04	21.79 $\pm$ 0.00	326.23 $\pm$ 0.00	2.94 $\pm$ 0.00	3.28 $\pm$ 0.00	0.64 $\pm$ 0.00
CNMF	2.13 $\pm$ 0.10	24.05 $\pm$ 0.21	241.72 $\pm$ 5.39	2.33 $\pm$ 0.07	1.68 $\pm$ 0.04	0.60 $\pm$ 0.01
HySure	22.70 $\pm$ 0.43	24.82 $\pm$ 0.28	241.17 $\pm$ 3.31	2.33 $\pm$ 0.13	3.25 $\pm$ 0.05	0.64 $\pm$ 0.01
FUMI	<b>0.12 <math>\pm</math> 0.02</b>	24.71 $\pm$ 0.00	242.25 $\pm$ 0.00	2.27 $\pm$ 0.00	3.19 $\pm$ 0.00	0.66 $\pm$ 0.00
GLP	2.36 $\pm$ 0.07	20.24 $\pm$ 0.00	403.70 $\pm$ 0.00	3.47 $\pm$ 0.00	3.14 $\pm$ 0.00	0.49 $\pm$ 0.00
MAPSMM	10.63 $\pm$ 0.21	18.35 $\pm$ 0.00	519.28 $\pm$ 0.00	4.30 $\pm$ 0.00	3.36 $\pm$ 0.00	0.42 $\pm$ 0.00
SFIM	0.20 $\pm$ 0.02	19.74 $\pm$ 0.00	423.46 $\pm$ 0.00	3.68 $\pm$ 0.00	3.31 $\pm$ 0.00	0.48 $\pm$ 0.00
Lanaras's method	2.82 $\pm$ 1.69	<b>29.59 <math>\pm</math> 0.71</b>	<b>149.59 <math>\pm</math> 13.20</b>	<b>1.19 <math>\pm</math> 0.09</b>	<b>1.43 <math>\pm</math> 0.06</b>	0.76 $\pm$ 0.05
Dataset - AVIRIS Indian Pines - No added noise						
MR- $\beta = 2$ -NMF	14.55 $\pm$ 0.07	36.43 $\pm$ 0.15	69.71 $\pm$ 1.65	0.65 $\pm$ 0.02	1.23 $\pm$ 0.03	0.92 $\pm$ 0.00
MR- $\beta = 3/2$ -NMF	15.69 $\pm$ 0.09	38.09 $\pm$ 0.09	57.69 $\pm$ 0.89	0.48 $\pm$ 0.00	1.00 $\pm$ 0.02	0.93 $\pm$ 0.00
MR- $\beta = 1$ -NMF	14.56 $\pm$ 0.03	39.30 $\pm$ 0.13	51.66 $\pm$ 0.79	0.41 $\pm$ 0.01	0.90 $\pm$ 0.01	0.94 $\pm$ 0.00
MR- $\beta = 1/2$ -NMF	16.00 $\pm$ 0.05	<u>39.15 <math>\pm</math> 0.20</u>	<u>52.98 <math>\pm</math> 1.18</u>	<u>0.42 <math>\pm</math> 0.01</u>	0.91 $\pm$ 0.02	0.94 $\pm$ 0.00
GSA	0.29 $\pm$ 0.03	23.33 $\pm$ 0.00	300.32 $\pm$ 0.00	2.42 $\pm$ 0.00	1.38 $\pm$ 0.00	0.90 $\pm$ 0.00
CNMF	1.94 $\pm$ 0.09	26.72 $\pm$ 0.16	184.42 $\pm$ 2.95	1.71 $\pm$ 0.04	1.17 $\pm$ 0.03	0.74 $\pm$ 0.01
HySure	20.83 $\pm$ 0.17	<b>40.96 <math>\pm</math> 0.03</b>	<b>44.29 <math>\pm</math> 0.18</b>	<b>0.34 <math>\pm</math> 0.00</b>	<b>0.56 <math>\pm</math> 0.00</b>	<b>0.96 <math>\pm</math> 0.00</b>
FUMI	<b>0.11 <math>\pm</math> 0.02</b>	39.13 $\pm$ 0.00	115.58 $\pm$ 0.00	0.83 $\pm$ 0.00	0.90 $\pm$ 0.00	0.95 $\pm$ 0.00
GLP	2.24 $\pm$ 0.05	23.12 $\pm$ 0.00	312.46 $\pm$ 0.00	2.48 $\pm$ 0.00	1.42 $\pm$ 0.00	0.85 $\pm$ 0.00
MAPSMM	10.09 $\pm$ 0.14	22.27 $\pm$ 0.00	346.40 $\pm$ 0.00	2.74 $\pm$ 0.00	1.54 $\pm$ 0.00	0.78 $\pm$ 0.00
SFIM	0.18 $\pm$ 0.01	22.66 $\pm$ 0.00	328.92 $\pm$ 0.00	2.62 $\pm$ 0.00	1.39 $\pm$ 0.00	0.85 $\pm$ 0.00
Lanaras's method	2.05 $\pm$ 1.90	29.89 $\pm$ 0.54	155.03 $\pm$ 7.39	1.15 $\pm$ 0.06	1.18 $\pm$ 0.02	0.81 $\pm$ 0.00

multiplicative updates to tackle the minimization problem and we showed that MR- $\beta$ -NMF is flexible and can be successfully applied to various problems. In particular, we have showcased its efficiency on two instrumental examples. The first is the audio spectral unmixing for which the frequency-by-time data matrix is computed with the short-time Fourier transform and is the result of a trade-off between the frequency resolution and the temporal resolution. We highlighted the capacity of this model to provide solutions that show high frequency and high temporal accuracy taking advantage from the input data. Based on these results, MR- $\beta$ -NMF seems to be well suited for audio applications such as transcription problems and performs in general better than baseline NMF methods. The second is blind hyperspectral unmixing for which the wavelength-by-location data matrix is a trade-off between the number of wavelengths measured and the spatial resolution. We demonstrated the efficiency of MR- $\beta$ -NMF to tackle the HS-MS data fusion problem. Based on various quantitative quality assessments, the proposed method performs competitively with the state of the art.

#### ACKNOWLEDGMENT

The authors would like to thank Andersen M.S. Ang for the help given for the generation of the audio signals used in this paper, and Xavier Siebert for his insightful comments that helped us improve the paper.

#### REFERENCES

- [1] J. Price, "Combining panchromatic and multispectral imagery from dual resolution satellite instruments," *Remote Sens. Environ.*, vol. 21, no. 2, pp. 119–128, 1987.
- [2] A. Gillespie, A. Kahle, and R. Walker, "Color enhancement of highly correlated images—ii channel ratio and 'chromacity' transformation techniques," *Remote Sens. Environ.*, vol. 22, no. 3, pp. 343–365, 1987.
- [3] W. Carper, T. Lillesand, and R. Kiefer, "The use of intensity-hue-saturation transform for merging spot panchromatic and multispectral image data," *Photogramm. Eng. Remote Sens.*, vol. 56, no. 4, pp. 459–467, 1990.
- [4] P. Chavez, S. Sides, and J. Anderson, "Comparison of three different methods to merge multiresolution and multispectral data: Landsat tm and spot panchromatic," *Photogramm. Eng. Remote Sens.*, vol. 57, no. 3, pp. 265–303, 1991.
- [5] R. Nishii, S. Kusanobu, and S. Tanaka, "Enhancement of low spatial resolution image based on high resolution bands," *IEEE Transactions on Geoscience and Remote Sensing*, vol. 34, no. 5, pp. 1151–1158, 1996.
- [6] T. Ranchin and L. Wald, "Fusion of high spatial and spectral resolution images: The arsis concept and its implementation," *Photogramm. Eng. Remote Sens.*, vol. 66, no. 1, pp. 49–61, 2000.
- [7] B. Aiazzi, L. Alparone, S. Baronti, and A. Garzelli, "Context-driven fusion of high spatial and spectral resolution images based on oversampled multiresolution analysis," *IEEE Transactions on Geoscience and Remote Sensing*, vol. 40, no. 10, pp. 2300–2312, 2002.
- [8] Q. Wei, J. Bioucas-Dias, N. Dobigeon, and J. Tourneret, "Hyperspectral and multispectral image fusion based on a sparse representation," *IEEE Transactions on Geoscience and Remote Sensing*, vol. 53, no. 7, pp. 3658–3668, 2015.
- [9] C. I. Kanatsoulis, X. Fu, N. D. Sidiropoulos, and W. Ma, "Hyperspectral super-resolution: A coupled tensor factorization approach," *IEEE Transactions on Signal Processing*, vol. 66, no. 24, pp. 6503–6517, 2018.
- [10] N. Yokoya, T. Yairi, and A. Iwasaki, "Coupled nonnegative matrix factorization unmixing for hyperspectral and multispectral data fusion," *IEEE Transactions on Geoscience and Remote Sensing*, vol. 50, no. 2, pp. 528–537, 2012.
- [11] D. Lee and H. Seung, "Learning the parts of objects by non-negative matrix factorization," *Nature*, vol. 401, no. 6755, p. 788, 1999.
- [12] C. Févotte and J. Idier, "Algorithms for nonnegative matrix factorization with the  $\beta$ -divergence," *Neural computation*, vol. 23, no. 9, pp. 2421–2456, 2011.
- [13] H. Kameoka, "Multi-resolution signal decomposition with time-domain spectrogram factorization," in *2015 IEEE International Conference on Acoustics, Speech and Signal Processing (ICASSP)*, 2015, pp. 86–90.
- [14] H. Kameoka, H. Kagami, and M. Yukawa, "Complex nmf with the

- generalized kullback-leibler divergence,” in *2017 IEEE International Conference on Acoustics, Speech and Signal Processing (ICASSP)*, 2017, pp. 56–60.
- [15] C. Févotte and M. Kowalski, “Estimation with low-rank time-frequency synthesis models,” *IEEE Transactions on Signal Processing*, vol. 66, no. 15, pp. 4121–4132, 2018.
  - [16] V. Leplat, N. Gillis, and A. M. S. Ang, “Blind audio source separation with minimum-volume beta-divergence nmf,” *IEEE Transactions on Signal Processing*, vol. 68, pp. 3400–3410, 2020.
  - [17] N. Gillis, “The why and how of nonnegative matrix factorization,” *Regularization, Optimization, Kernels, and Support Vector Machines*, vol. 12, no. 257, pp. 257–291, 2014.
  - [18] X. Fu, K. Huang, N. D. Sidiropoulos, and W. Ma, “Nonnegative matrix factorization for signal and data analytics: Identifiability, algorithms, and applications,” *IEEE Signal Processing Magazine*, vol. 36, no. 2, pp. 59–80, 2019.
  - [19] N. Yokoya, N. Mayumi, and A. Iwasaki, “Cross-calibration for data fusion of eo-1/hyperion and terra/aster,” *IEEE J. Sel. Topics Appl. Earth Observ. Remote Sens.*, vol. 6, no. 2, pp. 419–426, 2013.
  - [20] M. Simoes, J. Bioucas-Dias, L. B. Almeida, and J. Chanussot, “A convex formulation for hyperspectral image superresolution via subspace-based regularization,” *IEEE Trans. Geosci. Remote Sens.*, vol. 5, no. 2, pp. 3373–3388, 2015.
  - [21] J. Bioucas-Dias, A. Plaza, N. Dobigeon, M. Parente, Q. Du, P. Gader, and J. Chanussot, “Hyperspectral unmixing overview: Geometrical, statistical, and sparse regression-based approaches,” *IEEE Journal of Selected Topics in Applied Earth Observations and Remote Sensing*, vol. 5, no. 2, pp. 354–379, 2012.
  - [22] P. Smaragdis, C. Fvotte, G. J. Mysore, N. Mohammadiha, and M. Hoffman, “Static and dynamic source separation using nonnegative factorizations: A unified view,” *IEEE Signal Processing Magazine*, vol. 31, no. 3, pp. 66–75, 2014.
  - [23] N. Yokoya, C. Grohnfeldt, and J. Chanussot, “Hyperspectral and multispectral data fusion: a comparative review of the recent literature,” *IEEE Geoscience and Remote Sensing Magazine*, vol. 5, no. 2, pp. 29–56, 2017.
  - [24] C. Févotte, N. Bertin, and J.-L. Durrieu, “Nonnegative matrix factorization with the Itakura-Saito divergence: With application to music analysis,” *Neural computation*, vol. 21, no. 3, pp. 793–830, 2009.
  - [25] A. Lefèvre, “Méthode d’apprentissage de dictionnaire pour la séparation de sources audio avec un seul capteur,” Ph.D. dissertation, Ecole Normale Supérieure de Cachan, 2012.
  - [26] C. Févotte and N. Dobigeon, “Nonlinear hyperspectral unmixing with robust nonnegative matrix factorization,” *IEEE Transactions on Image Processing*, vol. 24, no. 12, pp. 4810–4819, 2015.
  - [27] Y. Sun, P. Babu, and D. Palomar, “Majorization-minimization algorithms in signal processing, communications, and machine learning,” *IEEE Transactions on Signal Processing*, vol. 65, no. 3, pp. 794–816, 2017.
  - [28] B. Aiazzi, S. Baronti, and M. Selva, “Improving component substitution pansharpening through multivariate regression of ms+pan data,” *IEEE Transactions on Geoscience and Remote Sensing*, vol. 45, no. 10, pp. 3230–3239, 2007.
  - [29] M. Simoes, J. Bioucas-Dias, L. Almeida, and J. Chanussot, “A convex formulation for hyperspectral image superresolution via subspace-based regularization,” *IEEE Trans. Geosci. Remote Sens.*, vol. 53, no. 6, pp. 3373–3388, 2015.
  - [30] Q. Wei, J. Bioucas-Dias, N. Dobigeon, J.-Y. Tourneret, M. Chen, and S. Godsill, “Multiband image fusion based on spectral unmixing,” *IEEE Transactions on Geoscience and Remote Sensing*, vol. 54, no. 12, pp. 7236–7249, 2016.
  - [31] B. Aiazzi, S. Alparone, S. Baronti, A. Garzelli, and M. Selva, “Mtf-tailored multiscale fusion of high-resolution ms and pan imagery,” *Photogrammetric Engineering and Remote Sensing*, vol. 72, no. 5, pp. 591–596, 2006.
  - [32] M. T. Eismann, “Resolution enhancement of hyperspectral imagery using maximum a posteriori estimation with a stochastic mixing model,” Ph.D. dissertation, Univ. Dayton, Dayton, OH, 2004.
  - [33] J. G. Liu, “Smoothing filter-based intensity modulation: a spectral preserve image fusion technique for improving spatial details,” *Int. J. Remote Sens.*, vol. 21, no. 18, pp. 3461–3472, 2000.
  - [34] C. Lanaras, E. Baltasvias, and K. Schindler, “Hyperspectral super-resolution by coupled spectral unmixing,” in *IEEE Int. Conf. Computer Vision*. IEEE, 2015, pp. 3586–3594.
  - [35] G. Vane, R. Green, T. Chrien, H. Enmark, E. Hansen, and W. Porter, “The airborne visible/infrared imaging spectrometer (aviris),” *Remote Sens. Environ.*, vol. 44, no. 2–3, pp. 127–143, 1993.
  - [36] L. Wald, “Quality of high resolution synthesised images: Is there a simple criterion?” in *Int. Conf. Fusion Earth Data*, 2000, pp. 99–105.
  - [37] J. Nascimento and J. Bioucas-Dias, “Summary of current radiometric calibration coefficients for landsat mss, tm, etm+, and eo-1 ali sensors,” *Remote Sens. Environ.*, vol. 113, no. 5, pp. 893–903, 2009.
  - [38] F. Zhu, “Hyperspectral unmixing: Ground truth labeling, datasets, benchmark performances and survey,” 2017.
  - [39] H. Su, Q. Du, and P. Du, “Hyperspectral image visualization using band selection,” *IEEE Journal of Selected Topics in Applied Earth Observations and Remote Sensing*, vol. 7, no. 6, pp. 2647–2658, 2014.
  - [40] J. Nascimento and J. Bioucas-Dias, “Vertex component analysis: A fast algorithm to unmix hyperspectral data,” *IEEE Trans. Geosci. Remote Sens.*, vol. 43, no. 4, pp. 898–910, 2005.
  - [41] J. Bioucas-Dias, “A variable splitting augmented lagrangian approach to linear spectral unmixing,” in *IEEE Workshop Hyperspectral Image and Signal Processing: Evolution Remote Sensing*. IEEE, 2009, pp. 1–4.
  - [42] L. Wald, “Quality of high resolution synthesised images: Is there a simple criterion?” in *Int. Conf. Fusion Earth Data*, 2000, pp. 99–103.
  - [43] Z. Wang and A. Bovik, “A universal image quality index,” *IEEE Signal Process. Lett.*, vol. 9, no. 3, pp. 81–84, 2002.
  - [44] L. Loncan, L. B. De Almeida, J. M. Bioucas-Dias, X. Briottet, J. Chanussot, N. Dobigeon, S. Fabre, W. Liao, G. Licciardi, and M. Simoes, “Hyperspectral pansharpening: A review,” *IEEE Geosci. Remote Sens. Mag.*, vol. 3, no. 4, pp. 27–46, 2015.